ChemComm

COMMUNICATION

View Article Online
View Journal | View Issue

Cite this: *Chem. Commun.*, 2023, 59, 2102

Received 6th December 2022,
Accepted 24th January 2023

DOI: 10.1039/d2cc06649a

rsc.li/chemcomm

Photocatalytic reductive C–O bond scission promoted by low-work-function Cd single atoms and clusters†

Lulu Sun, ‡[ab] Yike Huang,‡[ab] Shiyang Liu,[ab] Xiumei Liu,[a] Nengchao Luo *[a] and Feng Wang *[a]

C–O bond scission *via* photocatalysis is an important step in biomass depolymerization. Here, we demonstrate the scission of strong ether C–O bonds promoted by low-work-function Cd single atoms and clusters. Their loading on ZnS benefits C–H bond scission, thus weakening the C–O bond for chemical bond breaking.

Valorisation of natural biomass provides chemicals sustainably.[1,2] Cleaving the abundant C–O bonds is deemed to be significant to biomass depolymerization and an essential step in biomass refineries.[3,4] Because of the mild reaction conditions and the potential of being powered by solar energy,[4,5] photocatalysis has been demonstrated to be a powerful tool for C–O bond scission,[5,6] providing monomeric products selectively and beneficial to inhibiting recondensation.[7,8] The previous works of our group[9] and Wang[10] have individually proved that C–O bonds in β–O–4′ linkages in lignin can be reductively cleaved over semiconductor sulphides. The key is to weaken the C–O bonds as their reductive scission requires a very negative potential (generally lower than −1.6 V *vs.* standard hydrogen electrode).[11,12] Such methods highly rely on the prior scission of C–H bonds adjacent to the target C–O bonds. However, previous works reporting C–O bond scission are limited to cleaving benzylic C–H bonds because of the lower bond dissociation energy (BDE, ∼89 kcal mol^{-1}).[13] The type of C–O bond to be cleaved is restricted, adverse to obtaining monomeric products from lignin depolymerization.[14,15] Therefore, realizing selective and efficient scission of C–H bonds is important to the adjacent C–O bond scission. Low-work-function (LWF) metal nanoparticles supported on semiconductor sulphides have been reported to promote methanol C–H bond scission.[16] When sulphide is in contact with LWF metal nanoparticles, both the surface charge density and the energy structure of the sulphide are changed. More specifically, the electron transfer from LWF metal nanoparticles to the sulphide in the dark enriches the surface electrons while the immobilization of LWF metal nanoparticles promotes charge separation, thus conducive to accelerating C–H bond scission selectively. Besides preferential C–H bond scission, reductive C–O bond scission by simultaneously using photogenerated electrons cannot be overlooked.[17,18]

Because C–H bond scission has been successfully realised over CdS,[19] and Zn and Cd are in group IIB, here, we design a ZnS photo-catalyst supported with LWF Cd to inhibit the activation of the O–H bond, targeting the C–O bond scission of diethylene glycol (DEG) that has a similar skeleton structure to biomass feedstocks (Fig. S1, ESI†). We prove that the LWF Cd donates electrons to the ZnS support, which is deemed to be beneficial for the activation of the C–H bond rather than the O–H bond. The LWF Cd functions more brilliantly since the donated electrons are dispersed around LWF Cd clusters that act as the oxidation site for C–H bond scission. This electronic and band structure configuration facilitates DEG C–H bond scission, resulting in a carbon-centred radical capable of being reduced *via* C–O bond scission, thereby affording EG selectively.

DFT calculations verify the hypothesis of electron transfer from LWF Cd to ZnS supports. The electron transfer was evaluated by comparing the charge density of Cd and ZnS before and after contact. The obtained charge density difference (CDD) thus describes the electron transfer between the Cd and ZnS components. We considered the cases of Cd single atoms (Fig. 1a) and nanoclusters consisting of 10 Cd atoms (Fig. 1b and Fig. S2, ESI†). When either the LWF Cd single atom or the nanocluster is in contact with ZnS, the charge density of Cd and ZnS changes. More specifically, in the case of the Cd single atom, the electrons around Cd show a trend of deficiency while the electrons around the Zn^{2+} and S^{2-} become enriched. The electrons donated to ZnS are dispersed mainly around the S^{2-} though the electron density around part of the S^{2-} becomes

[a] *State Key Laboratory of Catalysis, Dalian National Laboratory for Clean Energy, Dalian Institute of Chemical Physics, Chinese Academy of Sciences, Dalian, 116023, China. E-mail: ncluo@dicp.ac.cn, wangfeng@dicp.ac.cn*

[b] *University of Chinese Academy of Sciences, Beijing, 100049, China*

† Electronic supplementary information (ESI) available: Experimental details and supplementary figures. See DOI: https://doi.org/10.1039/d2cc06649a

‡ These authors contributed to the work equally and should be regarded as co-first authors.

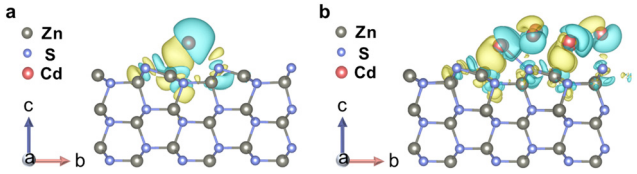

Fig. 1 Charge transfer between low-work-function Cd and ZnS. The charge density difference of ZnS supported with Cd single atoms (a) and Cd clusters (b). The yellow and cyan contours around the atoms represent enriched and deficient electron clouds, respectively, which describes the charge transfer of the ZnS support after contacting Cd single atoms and clusters, respectively.

deficient. The total electrons donated to ZnS were calculated to be 0.14 per Cd atom. Similar results are found for the Cd nanocluster, and the CDD describing the charge transfer of Cd/ZnS implies that the dominant electrons donated by Cd nanoclusters disperse around the interface of the Cd nanocluster and ZnS. The total electrons donated to ZnS are 0.08 per Cd atom. The above results indicate that Cd donates electrons to the ZnS support, resulting in a ZnS with enriched electrons conducive to DEG C–H bond scission.

We then prepared the Cd/ZnS material with the Cd in the form of single atoms and nanoclusters. This Cd/ZnS material was prepared by photo-irradiating a mixture containing fresh metallic Cd colloid and ZnS powder. The Cd content was determined to be 1.0 wt% by inductively coupled plasma atomic emission spectroscopy (ICP-AES). The morphology and structure of Cd/ZnS were characterized by scanning transmission electron microscopy (STEM) and X-ray diffraction (XRD). In the high-resolution TEM (HRTEM), the lattice fringes with distances of 0.255 and 0.265 nm are attributed to the (020) and (200) crystal planes of zinc blende, respectively (Fig. S3a, ESI†).[20] Besides, the lattice fringes with distances of 0.292 and 0.319 nm are attributed to the (101) and (002) crystal planes of wurtzite, respectively (Fig. S3b, ESI†).[20] Therefore, the synthesized ZnS is a mixed crystal phase containing zinc blende and wurtzite. Energy-dispersive X-ray spectroscopy (EDS) maps of the synthesized Cd/ZnS show the uniform distribution of S, Zn and Cd elements (Fig. S4, ESI†). The spherical aberration-corrected high-angle annular dark-field scanning transmission electron microscope (ac-HADDF-STEM) image of the Cd/ZnS shows uniformly dispersed bright spots on the ZnS surface, indicating the presence of Cd single atoms (Fig. 2a). We also found Cd nanoclusters on ZnS according to the line scan across the sample (Fig. 2b), since along this line, the relative abundance of S, Zn and Cd varies with Cd enriched in the cross-section of 7.5–17 nm (Fig. 2c). In accordance with this, the UV-visible diffuse reflectance spectrum (UV-vis DRS) shows an absorption peak near the edge for the Cd/ZnS sample (Fig. 2d), which might be derived from the localized surface plasma resonance of Cd.[21] The presence of Cd nanoclusters was further confirmed by X-ray diffraction (XRD). The series of peaks at 2θ degrees of 28.5°, 47.5° and 56.3° are indexed accordingly to zinc blende and wurtzite phases (Fig. 2e).[22] Besides these, diffraction peaks at 32.0°, 34.0° and 38.3° emerge for Cd/ZnS (Fig. 2e),

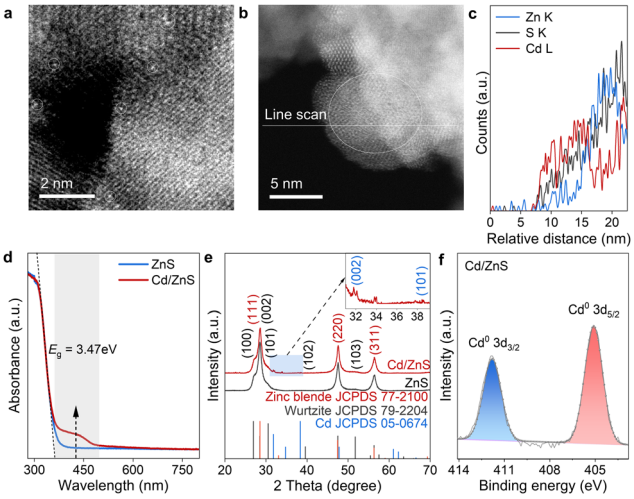

Fig. 2 Representative STEM, STEM-EDS elemental maps, UV-vis absorption spectroscopy, XRD and X-ray photoelectron spectroscopy patterns of ZnS and Cd/ZnS. STEM images of Cd/ZnS, showing the presence of Cd single atoms (a) and nanoclusters (b). (c) STEM-EDS elemental maps of S, Zn, and Cd along the white line in (c and d) Cd nanoparticles on the surface of ZnS enhance the light absorption ability of ZnS. (e) XRD patterns of Cd/ZnS in contrast to ZnS. (f) The Cd 3d binding energy of Cd/ZnS corresponds to the Cd^0.

which can be well indexed to hexagonal cadmium with the space group of *P*63/*mmc*, confirming the presence of Cd nanoclusters on ZnS. The Cd single atoms and clusters are in metallic states (Fig. 2f) according to the results of X-ray photoelectron spectroscopy (XPS).[23,24]

We choose the conversion of DEG, a model substrate of biomass, as the model reaction to shed light on the mechanisms of C–O bond breakage in biomass macromolecules. The photocatalytic DEG conversion was conducted to evaluate the promotional effects of Cd single atoms and nanoclusters on the activity of ZnS for C–O bond scission. DEG could be converted in mainly three pathways, including the initial scission of C_α–H, C_β–H and O–H bonds (Fig. 3a). The factors that influence the enthalpy, polarity, or steric configuration of the alcohols and photocatalyst should influence the selectivity of the initial DGE bond scission.[25–27] The target reaction pathway is the initial C_α–H bond scission, which generates carbon-centred radicals allowing for ether C–O bond scission under a mechanism analogous to the spin-centre-shift mechanism,[28] thus affording EG and acetaldehyde (AA). The initial C_β–H bond scission also generates a carbon-centred radical allowing for hydroxyl C–O bond scission, forming 2-(vinyloxy)ethan-1-ol (VEO) as the side product. The initial O–H bond scission is an unwanted reaction pathway, which finally affords 1, 4-dioxan-2-ol (DOO) as the side product. Photocatalytic DEG conversion over ZnS produces EG, AA and DOO with productivities of 1.22, 0.34 and 1.41 mmol g^{-1} in 10 h (Fig. 3b), respectively. The formation of EG and DOO confirms the scission of C_α–H and O–H bonds, respectively. The selectivity of EG and DOO is 47 and 53%, respectively, illustrating that O–H bond scission is prevalent over the ZnS photocatalyst. By

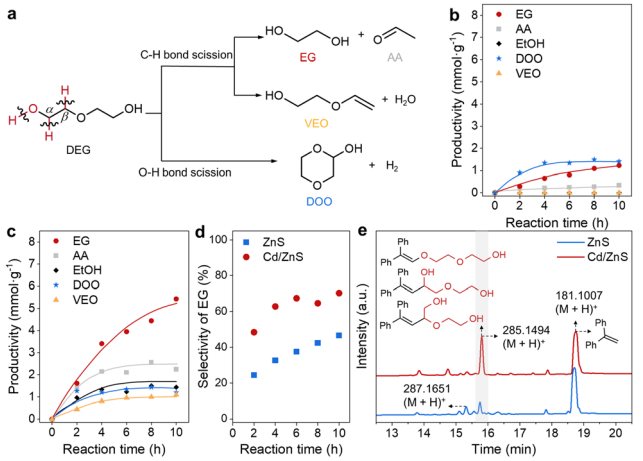

Fig. 3 Reaction results of photocatalytic cleavage of DEG to EG. (a) Reaction scheme of the photocatalytic DEG conversion over the Cd/ZnS photocatalyst. Time profiles recorded for the products from photocatalytic DEG conversion over ZnS (b) and Cd/ZnS (c). (d) Time profiles of EG selectivity. (e) Products of radical capturing experiments in photocatalytic DEG conversion analysed by LC-HRTOF-MS; 0.15 mmol of 1, 1-diphenylethylene was used as the radical capturing reagent. Standard conditions: 10 mg of ZnS or Cd/ZnS, 0.10 mL of DEG, 1.4 mL of MeCN, 5 W LEDs (365 ± 5 nm), 5 vol% CO/Ar, 2 h. A 5 vol% CO/Ar atmosphere was chosen to protect the metallic Cd from being oxidized.

comparison, reaction over Cd/ZnS generates EG, AA and DOO with productivities of 5.43, 2.25, and 1.20 mmol g^{-1}, respectively (Fig. 3c). The productivity of EG is substantially higher than that over ZnS, implying that the Cd promotes C_α–H bond scission. Besides the above three products, the photocatalytic DEG conversion over Cd/ZnS produces VEO with a productivity of 1.09 mmol g^{-1} in 10 h, suggesting that C_β–H bond scission also occurs. Since the C_α–H is adjacent to the active hydroxyl group, its scission is expected to be more facile than that for the C_β–H adjacent to the ether C–O bond.[29] The formation of VEO also implies that Cd/ZnS has a higher activity than ZnS. Ethanol, probably derived from the AA reduction by photogenerated electrons, is formed with a productivity of 1.50 mmol g^{-1}. For the reaction over Cd/ZnS, the selectivity of EG increases from 47 to 70% (Fig. 3d), substantially higher than that over ZnS, implying that Cd is beneficial for C_α–H bond scission. The selectivity of C–H bond scission (84%) for the reaction over DEG is also higher than that of O–H bond scission (16%, Fig. S5, ESI†), confirming a C–H bond breaking event promoted by LWF Cd single atoms and nanoclusters.

The stability of the Cd/ZnS photocatalyst was evaluated by catalyst recycling experiments (Fig. S6, ESI†). The spent Cd/ZnS photocatalyst deactivates in each run, especially for the activity of C–H bond scission. This result may be rationalized by the inevitable oxidation of metallic Cd during the recycling of the Cd/ZnS photocatalyst, and thus the promotional effects of Cd disappear. Photocatalytic cleavage of a β-O-4 lignin model compound (PP-ol) over Cd/ZnS was evaluated to illustrate that the found promotional effects of Cd can be expanded to biomass feedstocks (Fig. S7, ESI†). Compared with the reaction over ZnS, Cd/ZnS shows both higher conversion (82%) of PP-ol and selectivity for C–O bond scission (99%) for an irradiation time of 6 h, confirming the promotional effects of the metallic Cd in C–O bond scission initiated by C–H bond scission.

The involvement of photogenerated holes and electrons in the photocatalytic DEG cleavage was studied by control experiments using sacrificial reagents (Fig. S8, ESI†).[30] The addition of ferrocene and $AgNO_3$ as the sacrificial reagents for holes and electrons[30] dramatically decreases the productivities of all the products. This result agrees with a photocatalytic process requiring the co-participation of photogenerated holes and electrons. We then verify the reaction pathway of DEG C–O bond scission by radical capturing experiments, which were conducted by adding 1,1-diphenylethylene (DPE) to the reaction system. The products were analysed by liquid chromatography-high-resolution time-of-flight mass spectrometry (LC-HRTOF-MS). The signals of the chromatogram in Fig. 3e were recorded by a diode array detector. For the cases of ZnS and Cd/ZnS, the major found peaks with retention times around 15.8 and 18.7 min show *m*/*z* of 285.1494 and 181.1007. These two peaks, attributed to $(M + H)^+$ ions, suggest substances with molecule weights of 284 and 180, respectively. The latter is attributed to unreacted DPE while the former is related to the addition products of the radical derived from DEG C–H or O–H bond scission. After the radical addition to DPE, dehydrogenation of the addition products generates the substance with *m*/*z* of 284 (Fig. 3e).[31] We can also observe the addition products without dehydrogenation (*m*/*z* of 286) with a retention time of 15.3 min. Formation of the radical addition products implies that the C–O bond scission occurs *via* prior C–H bond scission (Fig. S9, ESI†). Besides, the larger peaks of the radical addition products imply that the improved activity of Cd/ZnS is derived from the higher activity for C–H bond scission.

We also found that Cd performs more brilliantly except for donating electrons to promote C–H bond scission. This critical role of Cd was further investigated by the density of states (DOS), describing the electron transfer upon light irradiation, using a ZnS (100) p (3 × 3 × 3) surface model and a Cd cluster consisting of 10 Cd atoms. The valence band maximum (VBM) of ZnS is constituted by S 3p and Zn 3d orbitals, with dominant contribution from Zn 3d. The conduction band minimum (CBM) is the hybrid of Zn 4s, Zn 3p, and Zn 3d orbitals (Fig. 4a), in agreement with the literature.[32] In comparison, the VBM of Cd/ZnS is constituted by S 3p, Zn 3d, and Cd 4d orbitals, with dominant contributions from Cd 4d (Fig. 4b). Although the Cd/ZnS CBM shows minor contributions from Cd 4d, the CBM components of Cd/ZnS and ZnS are similar. The VBM and CBM components of ZnS and ZnS supported by a single Cd atom are similar (Fig. S10a, ESI†). The above DOS results indicate that Cd clusters can substantially vary the band structure of ZnS.

The distribution of the VBM and CBM is displaced by plotting their contours in ZnS and Cd/ZnS lattices, which also dictates the transfer of photogenerated holes and electrons, respectively. For ZnS, the CBM distributes majorly in the bulk of the ZnS lattice while the VBM disperses almost evenly (Fig. S10b, ESI†). In comparison, the VBM and CBM of Cd/ZnS

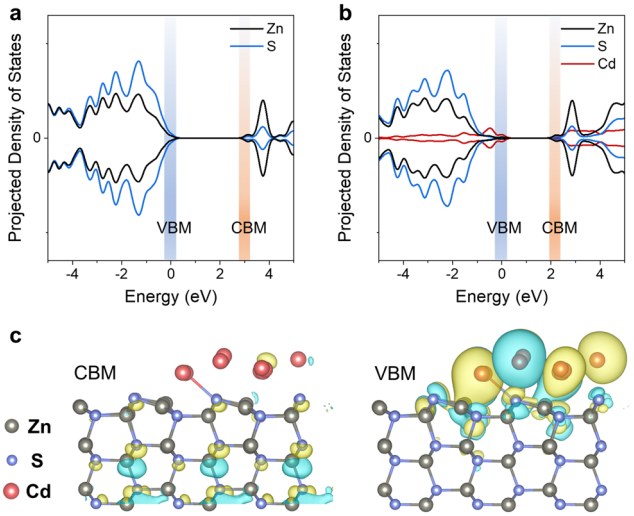

Fig. 4 DOS and contours of the band structure near the CBM and VBM. The DOS of ZnS (a) and Cd/ZnS (b). (c) The band structure near the CBM and VBM calculated for Cd/ZnS (ZnS supported with Cd clusters). The contours in yellow and cyan around the atoms represent two different electron spin states.

distribute differently (Fig. 4c). Although the contours depicting the distribution of the CBM are similar to that of ZnS, the VBM of Cd/ZnS almost concentrates around the Cd clusters and the interface of the Cd clusters and ZnS support. This configuration of VBM and CBM is beneficial for charge separation, with photogenerated hole migration to the surface, thereby beneficial for C–H bond oxidative cleavage for C–O bond scission.

In summary, we designed a ZnS photocatalyst supported with LWF Cd single atoms and nanoclusters. The LWF metallic Cd donates 0.08 electrons per Cd atom to the ZnS support, with electrons enriched around the interfacial S^{2-}. The electron-enriched ZnS support thus favours preferential scission of C–H bonds. Combining the preferential C–H bond scission and an analogous spin-center-shift mechanism, the C–O bond of the resulting carbon-centred radical was reduced by photo-generated electrons. Therefore, photocatalytic cleavage of DEG over Cd/ZnS shows improved activity and selectivity towards C–H bond scission. The mechanism study indicates that the DOS of Cd/ZnS shows better configuration than ZnS for charge separation and C–H bond scission, thanks to the localization of the VBM around the Cd clusters and the interface of the Cd clusters and ZnS support. This work provides a route for strong C–O bond scission, inspiring new strategies to depolymerize natural biomass.

This work was supported by the National Natural Science Foundation of China (22172157, 22002159, 22025206, 2172 1004), the Joint Fund of Yulin University and the Dalian National Laboratory for Clean Energy (Grant. YLU-DNL Fund 2021019), the Fundamental Research Funds for the Central Universities (20720220008), and K. C. Wong Education Foundation of Chinese Academy of Sciences (GJTD-2020-08). And we thank the instrumental support of the Liaoning Key Laboratory of Biomass Conversion for Energy and Material.

Conflicts of interest

There are no conflicts to declare.

Notes and references

1 L. F. Yan, Q. H. Zhang, W. P. Deng, Q. H. Zhang and Y. Wang, *Adv. Catal.*, 2020, **66**, 1–108.
2 W. P. Deng, Y. C. Feng, J. Fu, H. W. Guo, Y. Guo, B. X. Han, Z. C. Jiang, L. Z. Kong, C. Z. Li, H. C. Liu, P. T. T. Nguyen, P. N. Ren, F. Wang, S. Wang, Y. Q. Wang, Y. Wang, S. S. Wong, K. Yan, N. Yan, X. F. Yang, Y. H. Zhang, Z. R. Zhang, X. H. Zeng and H. Zhou, *Green Energy Environ.*, 2022, 10–114.
3 G. Magallanes, M. D. Kärkäs, I. Bosque, S. Lee, S. Maldonado and C. R. J. Stephenson, *ACS Catal.*, 2019, **9**, 2252–2260.
4 H. Chen, K. Wan, F. J. Zheng, Z. Zhang, Y. Y. Zhang and D. H. Long, *Renewable Sustainable Energy Rev.*, 2021, **147**, 111217.
5 C. Yang, M. D. Kärkäs, G. Magallanes, K. Chan and C. R. J. Stephenson, *Org. Lett.*, 2020, **22**, 8082–8085.
6 H. Luo, J. Barrio, N. Sunny, A. Li, L. Steier, N. Shah, I. E. L. Stephens and M. M. Titirici, *Adv. Energy Mater.*, 2021, **11**, 2101180.
7 A. Shivhare, D. Jampaiah, S. K. Bhargava, A. F. Lee, R. Srivastava and K. Wilson, *ACS Sustainable Chem. Eng.*, 2021, **9**, 3379–3407.
8 G. Q. Han, T. Yan, W. Zhang, Y. C. Zhang, D. Y. Lee, Z. Cao and Y. J. Sun, *ACS Catal.*, 2019, **9**, 11341–11349.
9 N. C. Luo, M. Wang, H. J. Li, J. Zhang, T. J. Hou, H. J. Chen, X. C. Zhang, J. M. Lu and F. Wang, *ACS Catal.*, 2017, **7**, 4571–4580.
10 X. J. Wu, X. T. Fan, S. J. Xie, J. C. Lin, J. Cheng, Q. H. Zhang, L. Y. Chen and Y. Wang, *Nat. Catal.*, 2018, **1**, 772–780.
11 F. Lin, H.-Y. Tse, H. C. Erythropel, P. V. Petrović, M. Garedew, J. Chen, J. C.-H. Lam and P. T. Anastas, *Green Chem.*, 2022, **24**, 6295–6305.
12 C. Yang, G. Magallanes, S. Maldonado and C. R. J. Stephenson, *J. Org. Chem.*, 2021, **86**, 15927–15934.
13 Y. Luo, *Comprehensive Handbook of Chemical Bond Energies*, CRC Press, 2007.
14 W. P. Deng, H. X. Zhang, L. Q. Xue, Q. H. Zhang and Y. Wang, *Chin. J. Catal.*, 2015, **36**, 1440–1460.
15 Z. L. Zhang, C. W. Lahive, D. S. Zijlstra, Z. W. Wang and P. J. Deuss, *ACS Sustainable Chem. Eng.*, 2019, **7**, 12105–12116.
16 N. C. Luo, W. Nei, J. J. Mu, S. Y. Liu, M. R. Li, J. Zhang, Z. Y. Gao, F. T. Fan and F. Wang, *ACS Catal.*, 2022, **12**, 6375–6384.
17 Q. Wang, J. Li, Y. Bai, J. Lian, H. Huang, Z. Li, Z. Lei and W. Shangguan, *Green Chem.*, 2014, **16**, 2728–2735.
18 T. Ben Nasr, N. Kamoun and C. Guasch, *Appl. Surf. Sci.*, 2008, **254**, 5039–5043.
19 X. J. Wu, X. T. Fan, S. J. Xie, J. C. Lin, J. Cheng, Q. H. Zhang, L. Y. Chen and Y. Wang, *Nat. Catal.*, 2018, **1**, 772–780.
20 S. S. J. Nanda and D. D. Sarma, *Chem. Mater.*, 2000, **12**, 1018–1024.
21 C. Kind and C. Feldmann, *Chem. Mater.*, 2011, **23**, 4982–4987.
22 S. A. Acharya, N. Maheshwari, L. Tatikondewar, A. Kshirsagar and S. K. Kulkarni, *Cryst. Growth Des.*, 2013, **13**, 1369–1376.
23 S. W. Gaarenstroom and N. Winograd, *J. Chem. Phys.*, 1977, **67**, 3500–3506.
24 J. S. Hammond, S. W. Gaarenstroom and N. Winograd, *Anal. Chem.*, 1975, **47**, 2193–2199.
25 Z. Y. Gao, N. C. Luo, Z. P. Huang, S. H. Taylor and F. Wang, *ACS Sustainable Chem. Eng.*, 2021, **9**, 6188–6202.
26 A. Ruffoni, R. C. Mykura, M. Bietti and D. Leonori, *Nat. Synth.*, 2022, **1**, 682–695.
27 Y. Chao, J. Lai, Y. Yang, P. Zhou, Y. Zhang, Z. Mu, S. Li, J. Zheng, Z. Zhu and Y. Tan, *Catal. Sci. Technol.*, 2018, **8**, 3372–3378.
28 T. Y. Peng, Z. Y. Xu, F. L. Zhang, B. Li, W. P. Xu, Y. Fu and Y. F. Wang, *Angew. Chem., Int. Ed.*, 2022, **61**, e202201329.
29 Q. Zhu and D. G. Nocera, *ACS Catal.*, 2021, **11**, 14181–14187.
30 Z. Hong, W. K. Chong, A. Y. R. Ng, M. Li, R. Ganguly, T. C. Sum and H. S. Soo, *Angew. Chem., Int. Ed.*, 2019, **58**, 3456–3460.
31 L. X. Shao, J. W. Huang and M. Shi, *Tetrahedron*, 2004, **60**, 11895–11901.
32 X. F. Lu, Q. F. Lei, X. Gao, J. Q. Ren, X. Guo and P. Q. La, *Phys. Status Solidi B*, 2018, **255**, 1800106.